# Figures and figure supplements

Structural basis for PRC2 decoding of active histone methylation marks H3K36me2/3
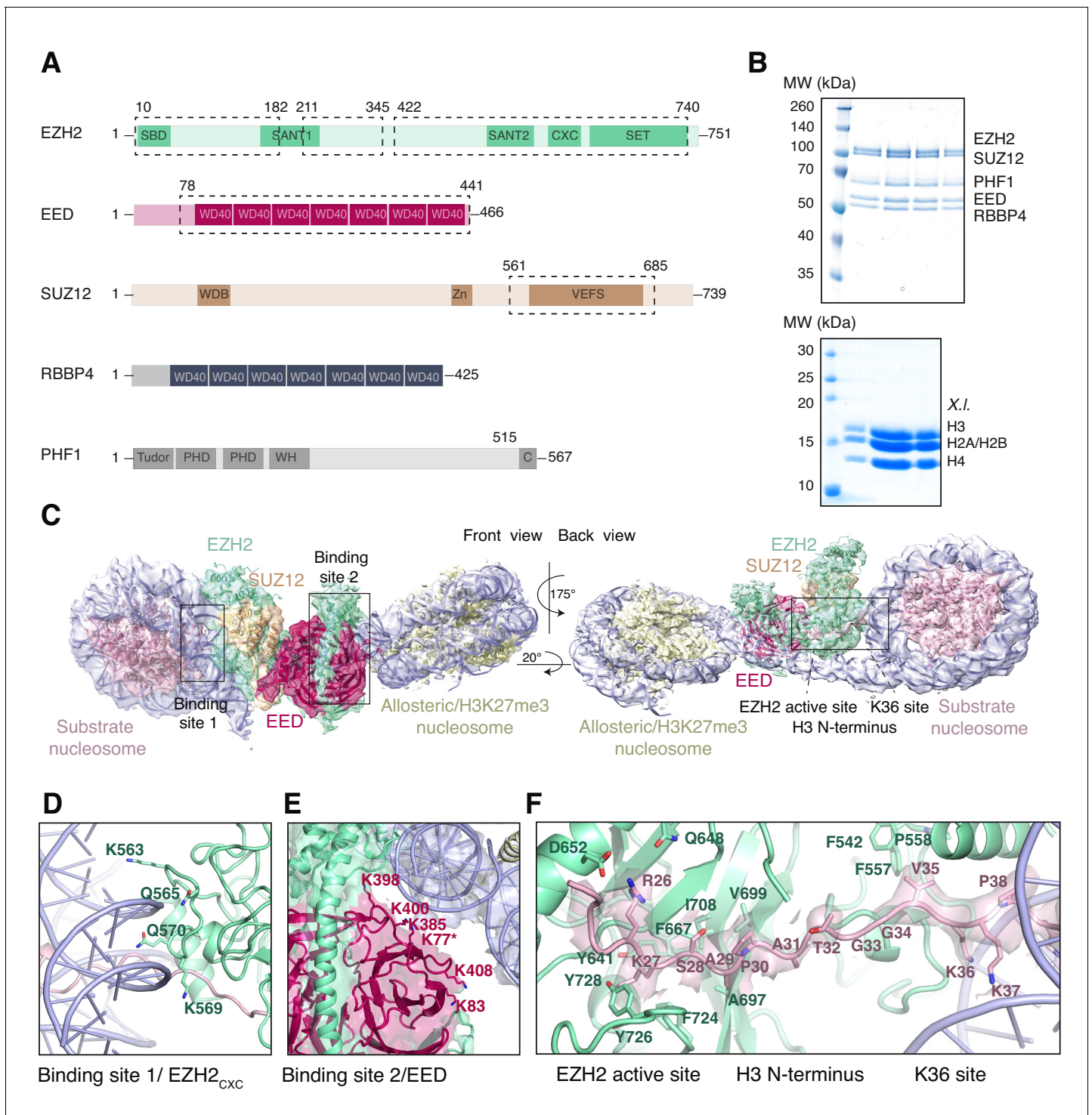
**Ksenia Finogenova** *et al*

**Figure 1.** Interaction of the PRC2 catalytic lobe with nucleosomal DNA orients the H3 N-terminus for H3K27 binding to the active site. (A) Domain organization in the five subunits of PHF1-PRC2. Dashed boxes indicate protein portions visible in the PHF1-PRC2:di-Nuc cryo-EM reconstruction and fitted in the structural model. In PHF1, C corresponds to the short C-terminal fragment used in PHF1$_C$-PRC2. (B) Coomassie-stained SDS PAGE analysis of representative PHF1-PRC2 (upper panel) and *Xenopus laevis* (*X.l.*) octamer preparations (lower panel) after size-exclusion chromatography (SEC) purification. Pooled fractions of PHF1-PRC2, incubated with heterodimeric dinucleosomes generated by DNA ligation of a reconstituted unmodified and a H3Kc27me3-modified mononucleosome as described in *Poepsel et al., 2018* were used as input material for cryo-EM analysis. (C) Cryo-EM reconstruction of PHF1-PRC2:di-Nuc in two orientations with fitted crystal structures of human PRC2 catalytic lobe (PDB: 5HYN, *Justin et al., 2016*) and nucleosomes (1AOI, *Luger et al., 1997*) in a di-Nuc model with 35 bp linker DNA (see also *Figure 1—figure supplements 1–4*, *Supplementary file 1*,

*Figure 1 continued on next page*

*Figure 1 continued*

*Figure 1—video 1*, *Source code 1*). Density is colored as in (**A**) to show PRC2 subunits, DNA (blue) and octamers of substrate (pink) and allosteric (yellow) nucleosomes. Boxes indicate regions shown in (**D**), (**E**) and (**F**), respectively. (**D**) Interaction of EZH2$_{CXC}$ residues with the DNA gyres of the substrate nucleosome; residues mutated in PRC2$^{CXC>A}$ are indicated. For the H3 N-terminus (pink), only the peptide backbone is shown in this view (see **F**). (**E**) Interface formed by EED and the EZH2 SBD domain with DNA gyres on the allosteric nucleosome; residues mutated in PRC2$^{EED>A}$ are indicated. Asterisk indicates the approximate location of a residue, which is not built in the model. (**F**) The H3 N-terminus (pink), shown as a pseudoatomic model fitted into the 4.4 Å density map, is recognized by EZH2 through an extensive interaction network (see text). Note the well-defined side-chain density of H3K36 (see also *Figure 1—figure supplement 3D* and *Figure 1—figure supplement 4C–E*).
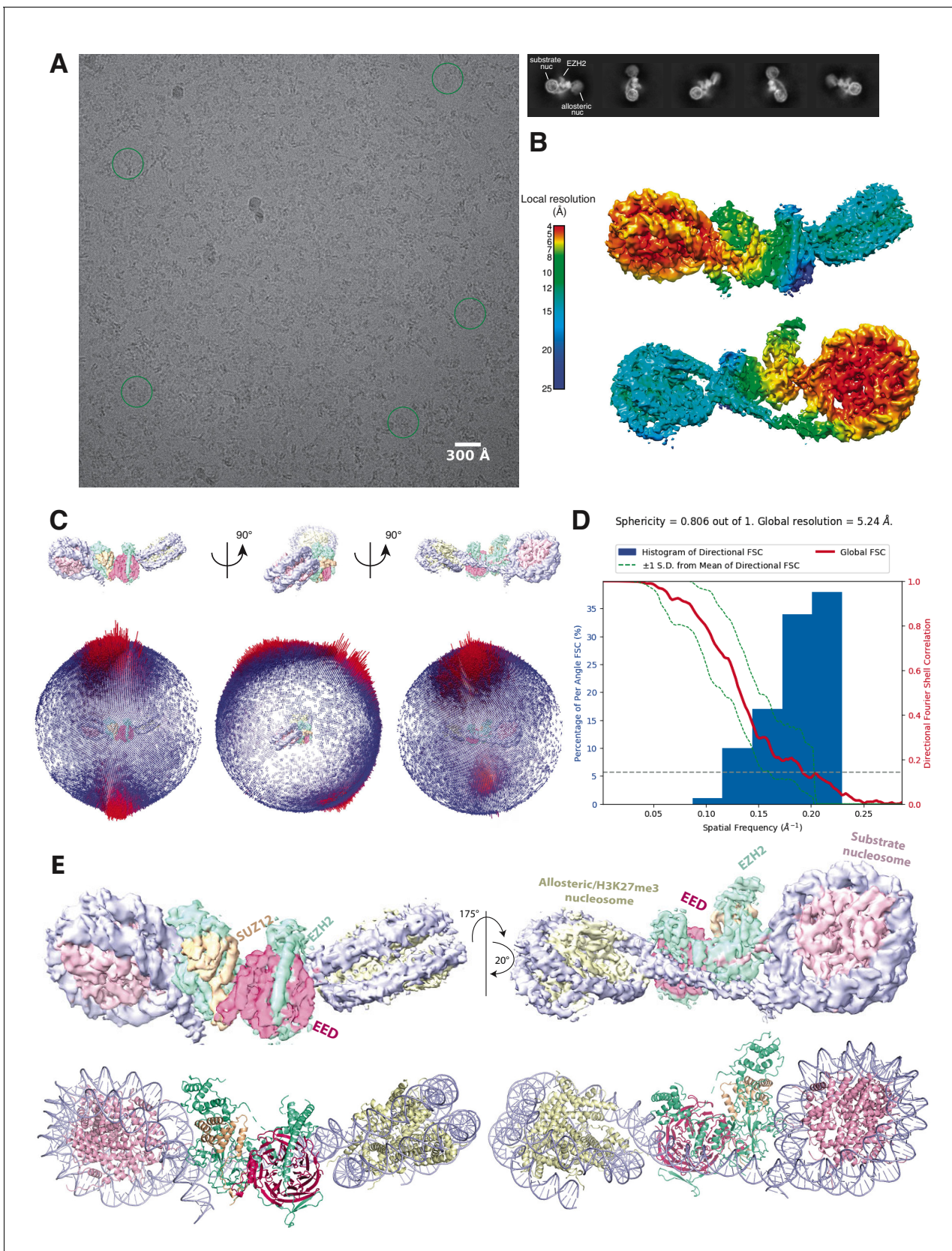
**Figure 1—figure supplement 1.** Initial Cryo-EM analysis of the PHF1-PRC2:di-Nuc complex (related to *Figure 1*). (**A**) Representative micrograph of the cryo-EM dataset (left) and reference-free 2D classes from particles picked without templates (right) (performed to ensure that no bias was introduced

*Figure 1—figure supplement 1 continued on next page*

*Figure 1—figure supplement 1 continued*

through templates picking and references in 3D classification). Circles indicate particles, which were picked with templates and directly subjected to 3D analysis (see *Figure 1—figure supplement 2*). (B) Local resolution estimation of the 5.2 Å overall PHF1-PRC2:di-Nuc map. The substrate nucleosome and the adjacent part of EZH2 are well resolved (colors red to yellow). (C) Spherical angular distribution of particles included in the final reconstruction of PHF1-PRC2:di-Nuc. (D) Output from the 3DFSC Processing Server (https://3dfsc.salk.edu/ *Tan et al., 2017*) showing the Fourier Shell Correlation (FSC) as a function of spatial frequency, generated from masked independent half maps of PRC2:diNuc: global FSC (red), directional FSC (blue histogram) and deviation from mean (spread, green dotted line). The nominal overall resolution of 5.24 Å was estimated according to the gold standard FSC cutoff of 0.143 (gray dotted line) (*Rosenthal and Henderson, 2003*). Sphericity is an indication for anisotropy and amounts to 0.806 in this data. The minor directional anisotropy of the data can be explained by the slightly preferred orientation and missing views as seen in (C). (E) Top: Refined and postprocessed cryo-EM density map of overall PHF1-PRC2:di-Nuc colored according to the subunit organization. Bottom: pseudoatomic model of fitted crystal structure of the human PRC2 catalytic lobe (PDB: 5HYN; *Justin et al., 2016*) and a di-Nuc model with 35 bp linker DNA (*Poepsel et al., 2018*), including PDB 1AOI (*Luger et al., 1997*).
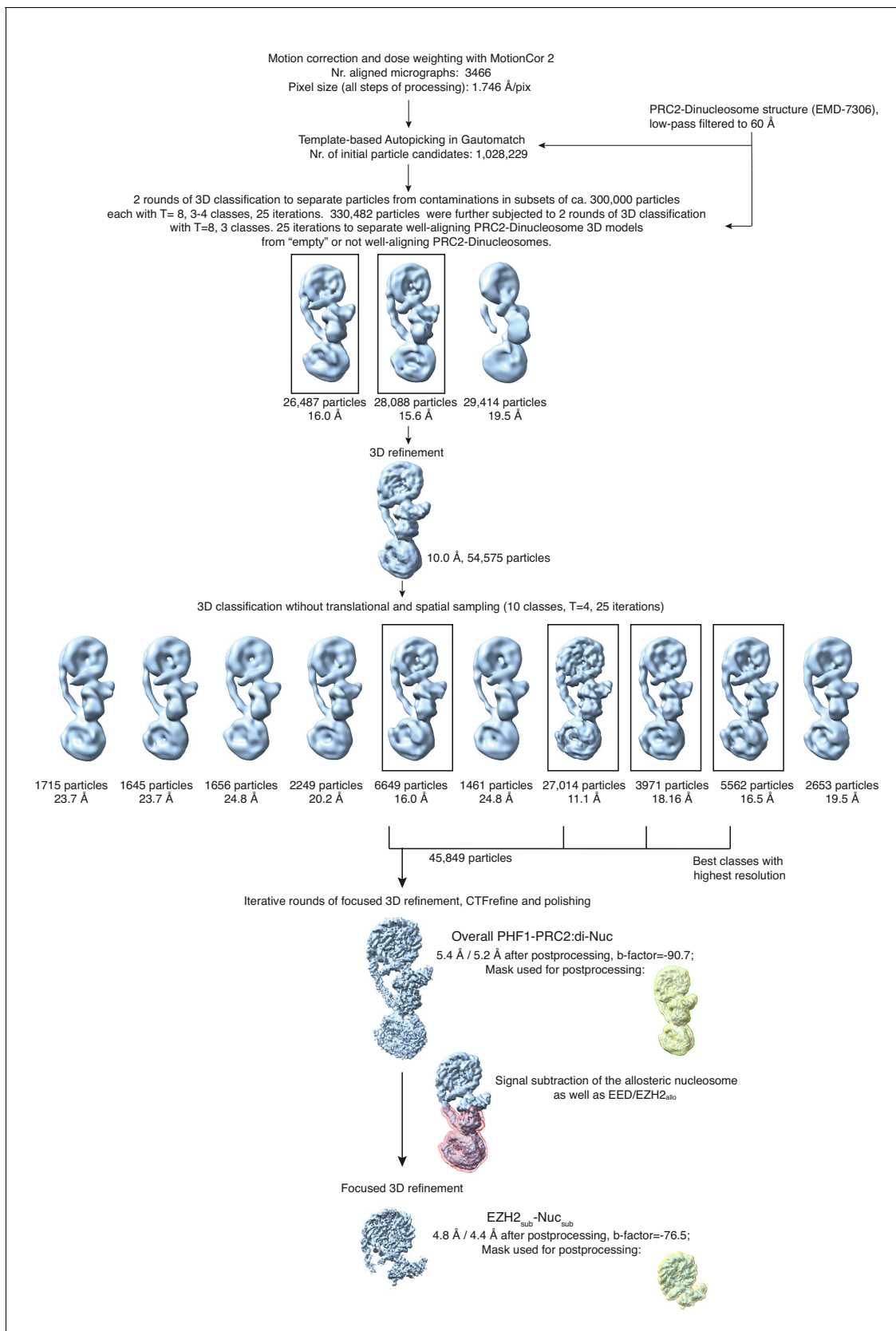
**Figure 1—figure supplement 2.** Overview of the cryo-EM Data-Processing and Particle Sorting Scheme (related to *Figure 1*). Processing and particle sorting scheme, also described in Methods. Squares indicate 3D classes (and corresponding particles) chosen for further processing steps based on

*Figure 1—figure supplement 2 continued on next page*

*Figure 1—figure supplement 2 continued*

their nominal global resolution values, translational and rotational accuracy and the presence of detailed structural information. Two final reconstructions were obtained in this study: Overall PHF1-PRC2:di-Nuc, and EZH2$_{sub}$-Nuc$_{sub}$ after performing signal subtraction (mask indicated in pink) and focused refinement. Masks used for postprocessing are shown in yellow.
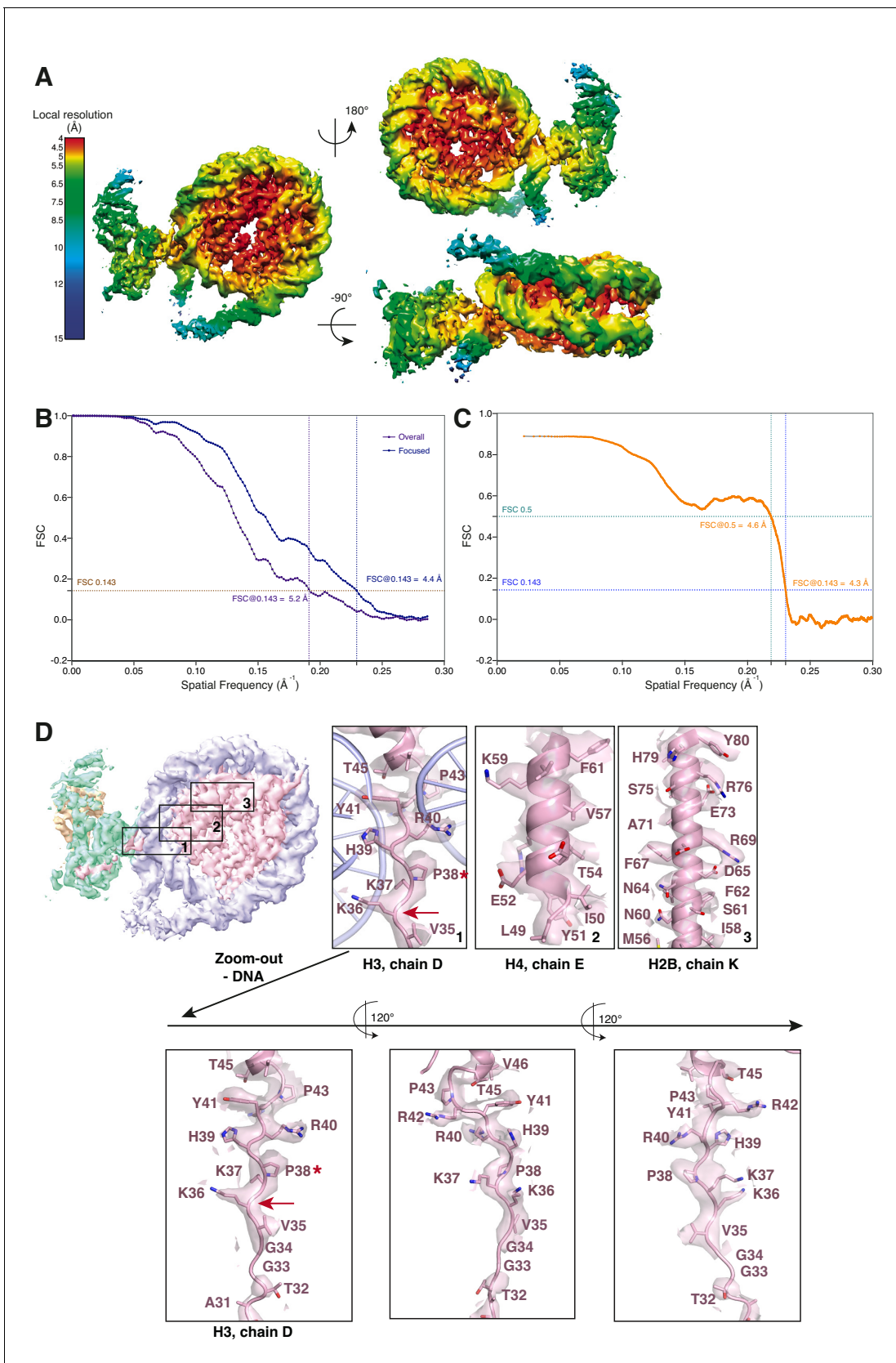
**Figure 1—figure supplement 3.** Cryo-EM analysis of the focused EZH2$_{sub}$-Nuc$_{sub}$ map (related to *Figure 1*). (**A**) Local resolution estimation of the focused 4.4 Å EZH2$_{sub}$:Nuc$_{sub}$ reconstruction. Regions in the nucleosome core as well as the adjacent regions including parts of the H3 N-terminus

*Figure 1—figure supplement 3 continued on next page*

*Figure 1—figure supplement 3 continued*

close to the exit side of the nucleosome are well resolved (4.0–5.5 Å). Regions close to the mask, especially the nucleosomal DNA and parts of EZH2, are less well resolved (colors green to blue). (B) Global FSC generated from masked independent half maps of $EZH2_{sub}$-$Nuc_{sub}$ (Focused, blue line) and the overall PHF1-PRC2:di-Nuc (Overall, violet line) were plotted against spatial frequency. The resolution of 4.4 Å for $EZH2_{sub}$-$Nuc_{sub}$ map and 5.2 Å for the overall PHF1-PRC2:di-Nuc map were estimated according to the gold standard FSC cutoff of 0.143 (brown dotted line) (*Rosenthal and Henderson, 2003*) (C) FSC between the atomic model and the masked (applied in Phenix) map of $EZH2_{sub}$-$Nuc_{sub}$ after real-space refinement (*Afonine et al., 2018*). Green line represents the cut-off at 0.5 (4.6 Å) and blue line represents the cut-off at 0.143 (4.3 Å) (see also *Supplementary file 1*; *Rosenthal and Henderson, 2003*; *Henderson et al., 2012*; *Rosenthal and Rubinstein, 2015*). (D) Selected regions within $EZH2_{sub}$-$Nuc_{sub}$ showing side-chain density, e.g. K36 (red arrow). A red asterisk indicates the last residue of the H3 tail visible in known crystal structures (usually P38 or H39). The quality of the map around K36 is shown as a separate zoom-out below and in three different views to demonstrate the lack of anisotropy present in the density.
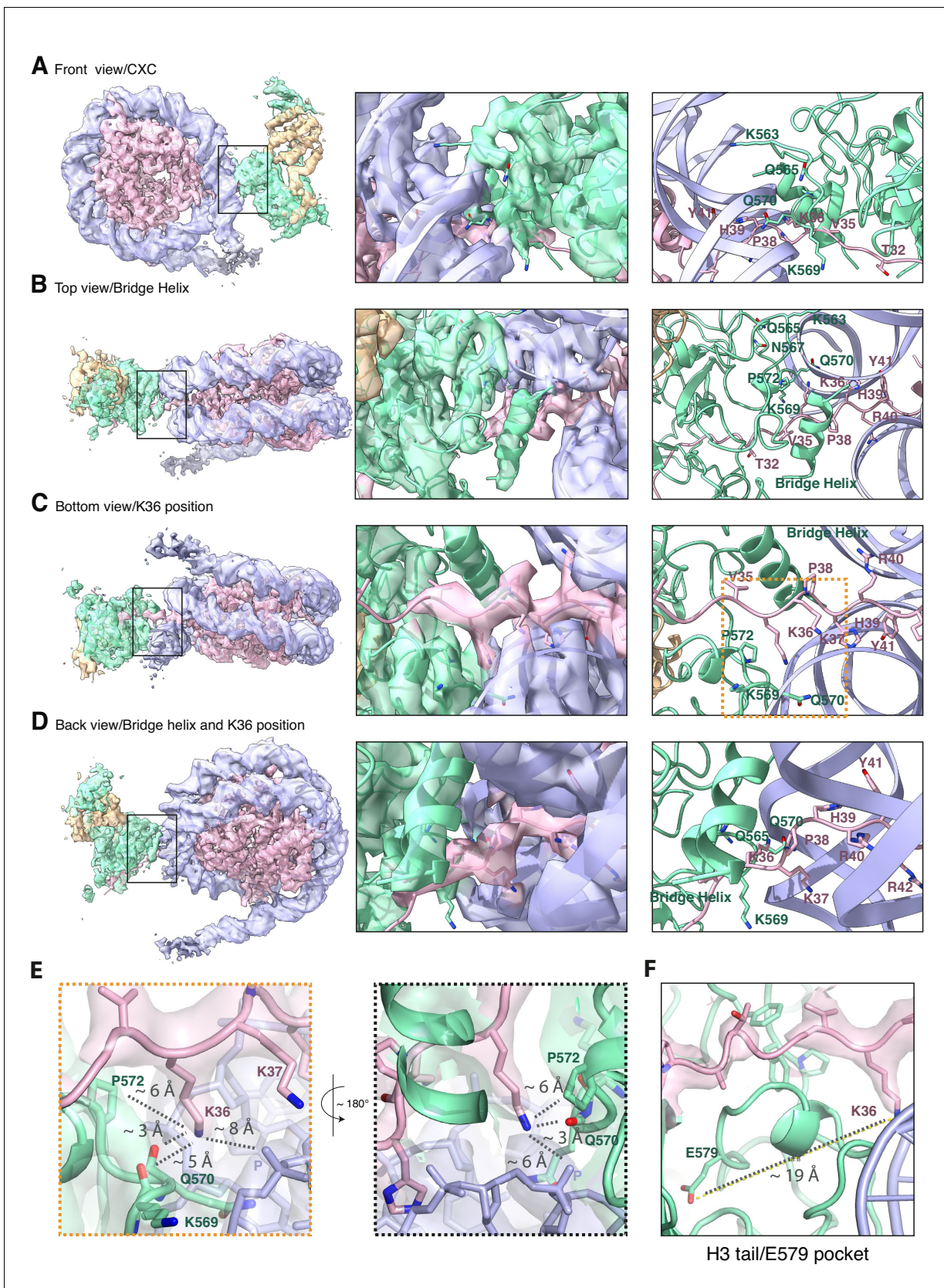
**Figure 1—figure supplement 4.** The improved map of the interaction between EZH2 and the substrate nucleosome after focused refinement reveals location of H3K36 and its environment (related to *Figure 1*). (A) The front view of EZH2sub-Nucsub cryo-EM density and model shows details of the

*Figure 1—figure supplement 4 continued*

EZH2$_{CXC}$ interaction with nucleosomal DNA. (B) The top view of EZH2$_{sub}$-Nuc$_{sub}$ cryo-EM shows a tubular density into which based on recent findings of the Nogales lab ( *Kasinath et al., 2020* ) an α-helix was built. The "bridge helix" (*Kasinath et al., 2020*) which based on this study is likely constituted of the EZH2 residues 497–511, is located above V35 of the H3 tail. As can be seen when observing the density-modified map (*Terwilliger et al., 2020*) of EZH2$_{sub}$-Nuc$_{sub}$ at lower threshold, it presumably engages in interactions with the nucleosomal DNA, the H3 tail and EZH2, as described in greater detail in *Kasinath et al., 2020*. (C) The bottom view of EZH2$_{sub}$-Nuc$_{sub}$ cryo-EM density and model shows details of the vicinity of K36 with the corresponding density for the H3 tail, EZH2 and nucleosomal DNA. The orange square indicates the region shown as a zoom-in in (E). (D) The back view of EZH2$_{sub}$-Nuc$_{sub}$ cryo-EM density and model shows details of the location of K36 and the "bridge helix" (*Kasinath et al., 2020* ). (E) Zoom-in views of H3K36 and its chemical environment. Approximate distances of the epsilon-amino group of H3K36 to the nearest residues are indicated with a dotted gray line. (F) Location of the Glu-579 pocket (*Jani et al., 2019*) in the EZH2$_{sub}$:Nuc$_{sub}$ reconstruction and its distance to H3K36 (app. 19 Å). The described mechanism by *Jani et al., 2019* involving recognition of H3K36 by Glu-579 is incompatible with the presented structural data as the location differs significantly and major rearrangements as the relocation of the helix-loop region between residues 564–576 would be necessary to avoid the given steric and geometric hindrance and allow for potential interaction.
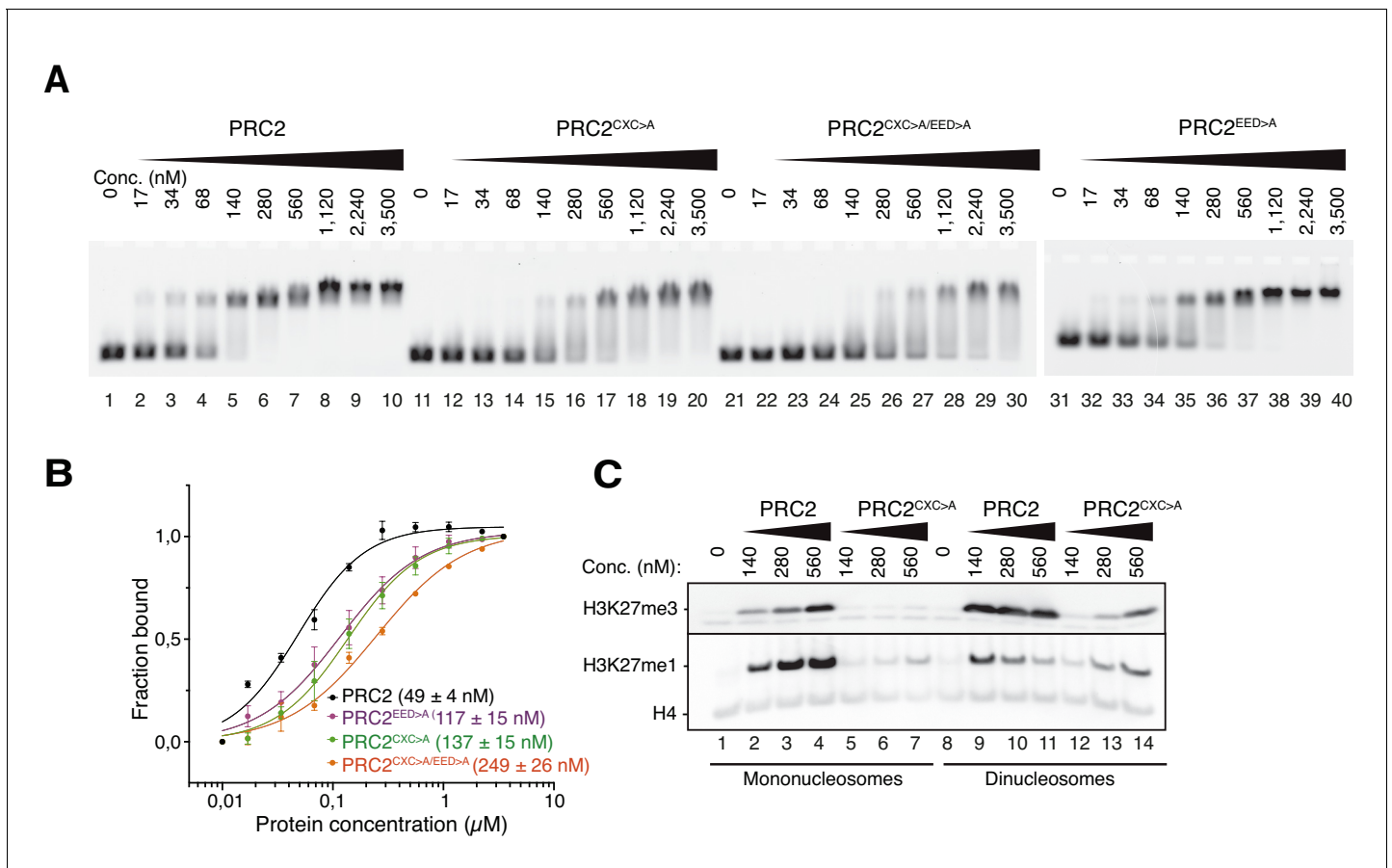
**Figure 2.** The EZH2$_{CXC}$-DNA interaction interface is critical for H3K27 methylation on nucleosomes. (**A**) Binding reactions with indicated concentrations of PRC2 (lanes 1–10), PRC2$^{CXC>A}$ (lanes 11–20), PRC2$^{CXC>A/EED>A}$ (lanes 21–30), or PRC2$^{EED>A}$ (lanes 31–40) and 45 nM 6-carboxyfluorescein-labeled mononucleosomes, analyzed by EMSA on 1.2% agarose gels. The EMSA with PRC2$^{EED>A}$ was run on a separate gel. (**B**) Quantitative analysis of EMSA data in A by densitometry of 6-carboxyfluorescein signals from independent experiments (n = 3); error bars, SEM. (**C**) Western Blot (WB) analysis of H3K27me1 and H3K27me3 formation in HMTase reactions with indicated concentrations of PRC2 and PRC2$^{CXC>A}$ on 446 nM mononucleosomes (lanes 1–7) or 223 nM dinucleosomes (lanes 8–14). Note that these concentrations result in equal numbers of nucleosomes and therefore equal numbers of H3 substrate molecules in the reactions on mono- and dinucleosomes, as can be seen from the Coomassie-stained gel of the reactions in *Figure 2—figure supplement 1B*. H4 WB signal served as control for western blot processing.
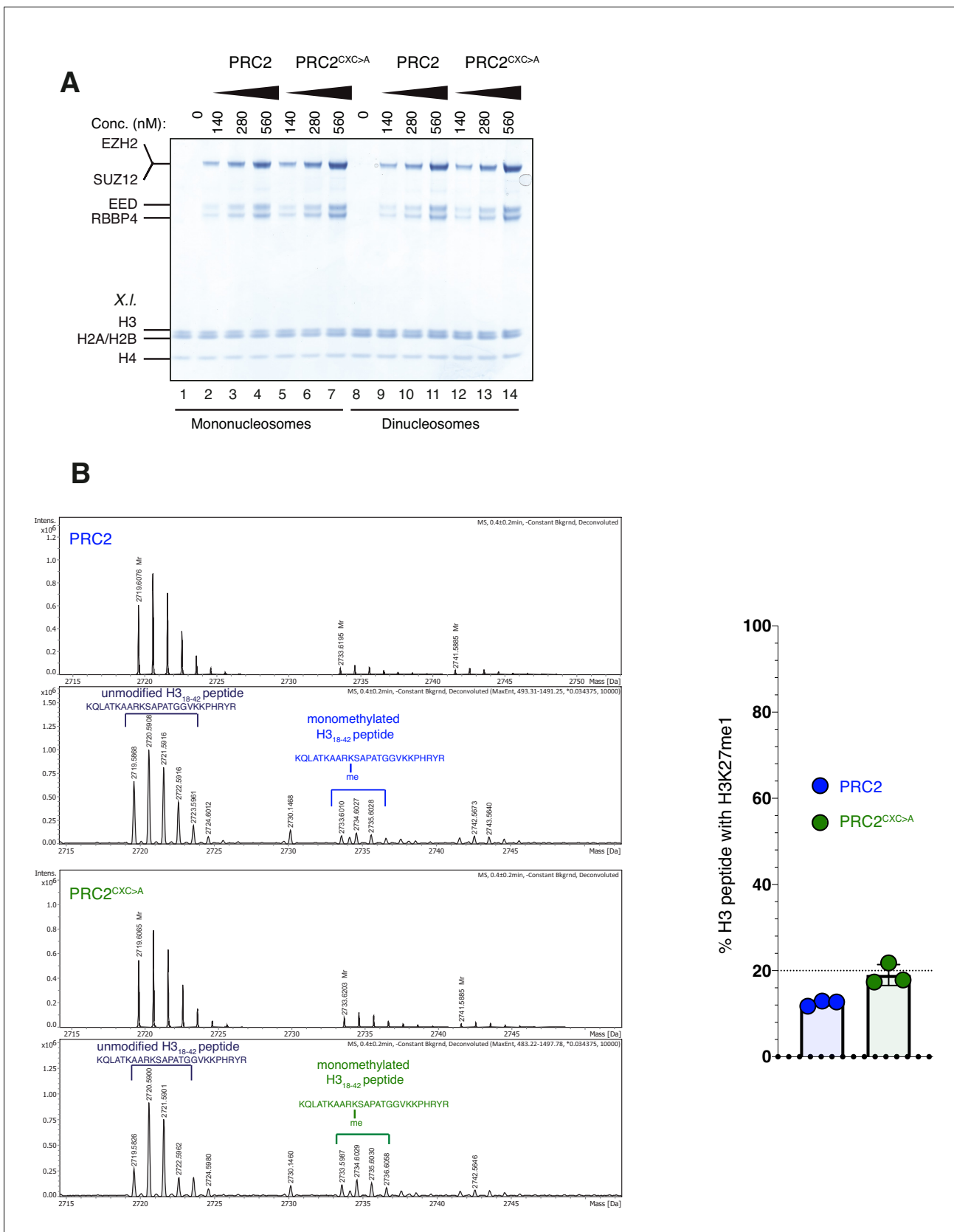
**Figure 2—figure supplement 1.** The EZH2$_{CXC}$-DNA interaction interface is critical for H3K27 methylation on nucleosomes (related to *Figure 2*). (A) Coomassie-stained 4–12% SDS-PAGE of the HMTase reactions shown in *Figure 2C*. *Xenopus laevis* (*X.l.*) nucleosomes were used for these experiments.

*Figure 2—figure supplement 1 continued on next page*

Figure 2—figure supplement 1 continued

The short 5 kDa PHF$_C$ fragment is not visible on this gel. (**B**) Left: Mass spectrometry-based HMTase assays monitoring H3K27me1 formation by PRC2 (blue; upper two panels) and PRC2$^{CXC>A}$ (green; lower two panels) on H3$_{18-42}$ peptides. Representative full ESI MS Spectra (top part) and deconvoluted spectra (lower part) are shown for the individual runs. For both runs, peaks indicated by the brackets were used for quantification of H3K27me1 formation. Right: Symbols represent percentages of peptides carrying H3K27me1 in technical triplicate experiments; error bars show SD.
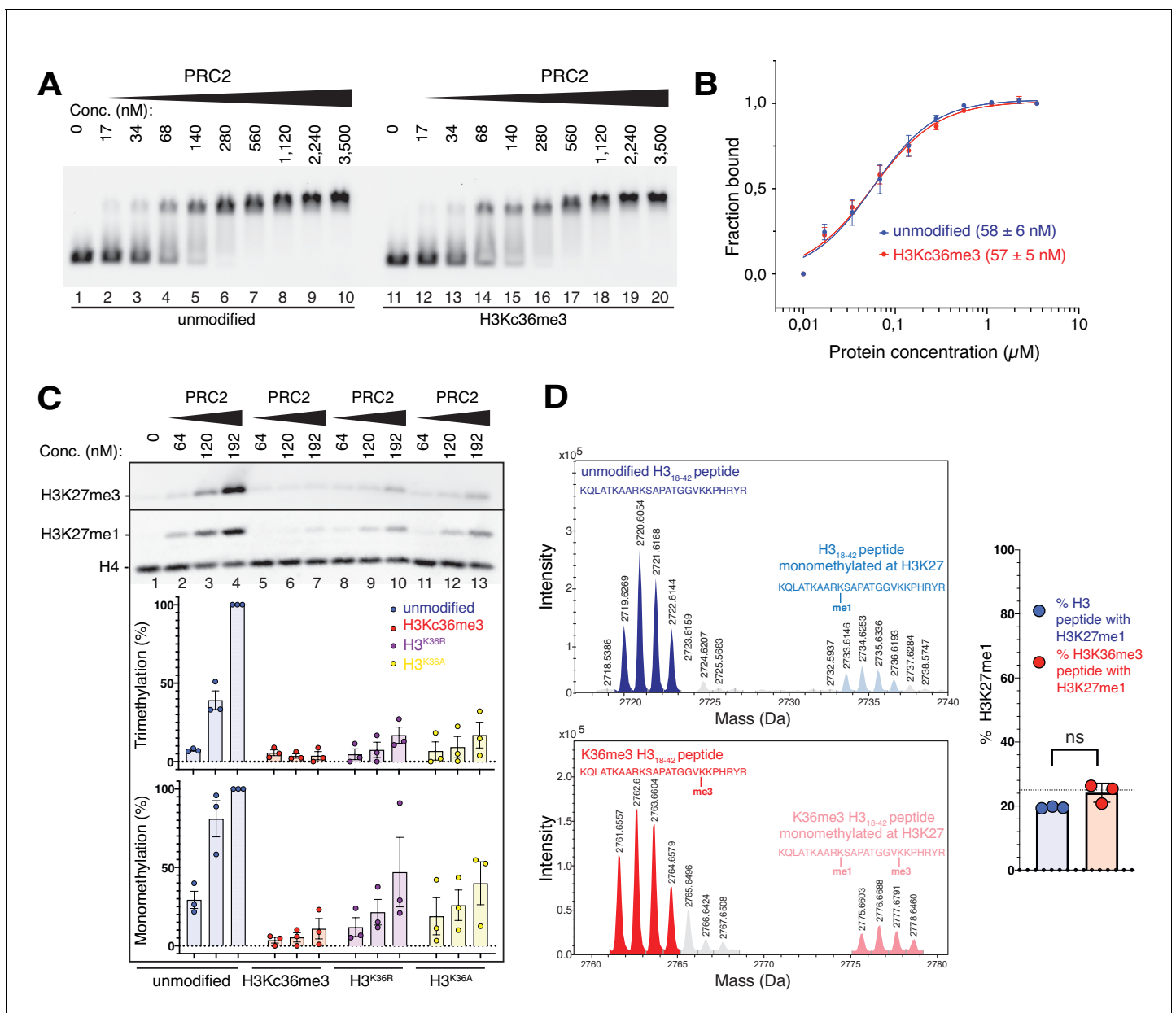
**Figure 3.** The unmodified H3K36 side chain in the EZH2$_{CXC}$-DNA interaction interface is critical for H3K27 methylation on nucleosomes. (A, B) EMSA analysis and quantification as in *Figure 2A and B*, using PRC2 and mononucleosomes that were unmodified (lanes 1–10) or contained a trimethyllysine analog at H3K36 (H3Kc36me3, lanes 11–20) (*Simon et al., 2007*). (C) Western blot (WB) analysis of HMTase reactions with PRC2 as in *Figure 2C* on unmodified (lanes 1–4), H3Kc36me3 (lanes 5–7), H3$^{K36R}$ (lanes 8–10) or H3$^{K36A}$ (lanes 11–13) mononucleosomes (446 nM). Coomassie-stained gel of reactions is shown in *Figure 3—figure supplement 1A*. Bottom: quantification of H3K27me3 and H3K27me1 chemiluminescence signals, respectively, by densiometry analysis from three independent experiments. In each experiment, the methylation signal in lane four was defined as 100% and used to quantify the corresponding H3K27 methylation signals in the other lanes on the same membrane. Circles show individual data points and error bars SEM. (D) HMTase reactions monitoring H3K27me1 formation by PRC2 on H3$_{18-42}$ peptides that were unmodified (top) or contained K36me3 (bottom). Left: Deconvoluted ESI-MS spectra from data shown in *Figure 3—figure supplement 1B*. On both substrates, areas of the four colored peaks of H3K27me1-modified and unmodified substrate peptides were used for quantification of H3K27me1 formation. Right: Symbols represent percentages of peptides carrying H3K27me1 in technical triplicate experiments, error bars show SD; Welch's t-test showed no significant (ns) difference between H3K27 monomethylation on the two peptide substrates.
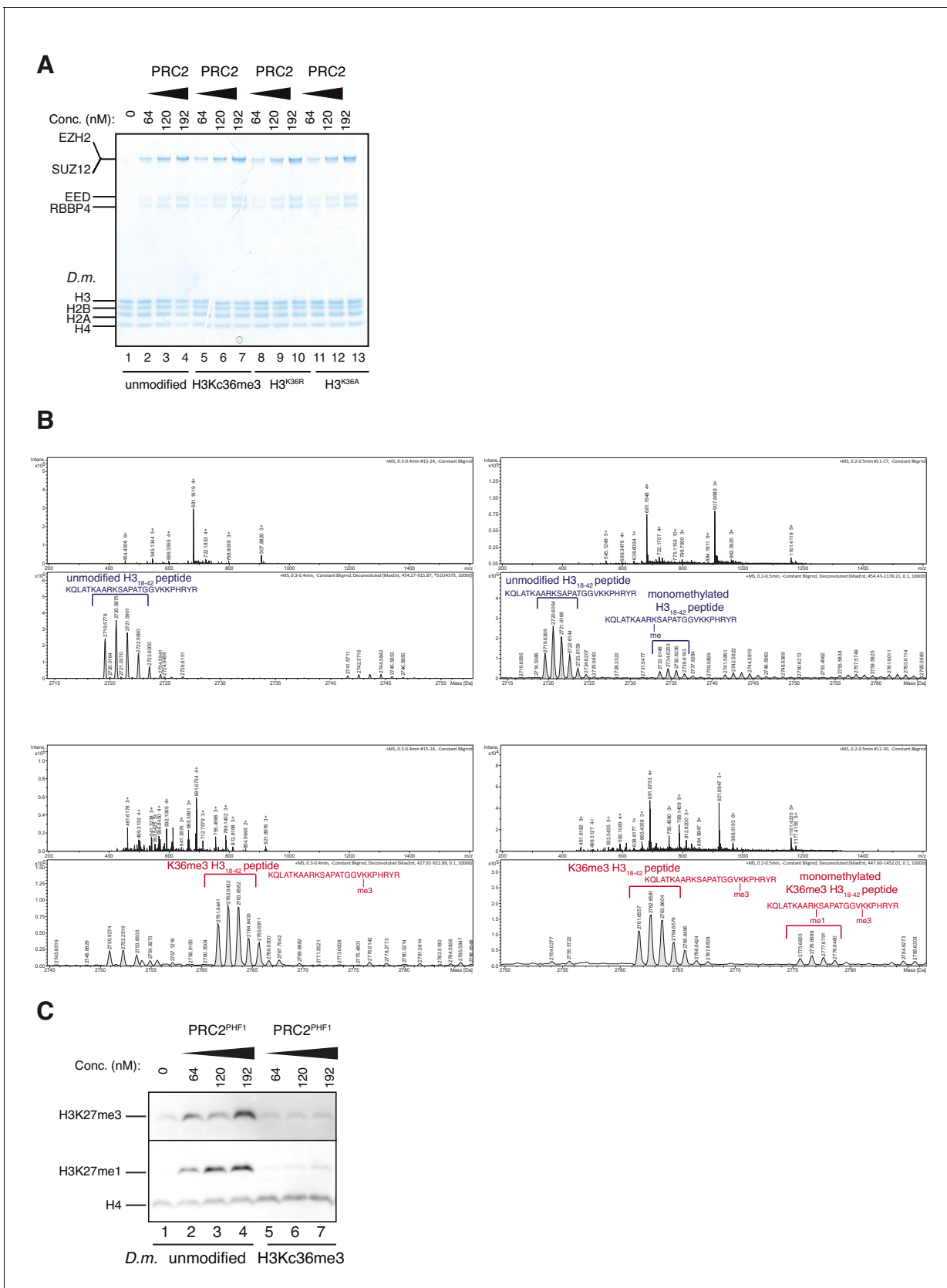
**Figure 3—figure supplement 1.** Accommodation of unmodified H3K36 in the EZH2$_{CXC}$-DNA interaction interface is essential for H3K27 methylation on nucleosomes and PHF1-PRC2 (related to *Figure 3*). (**A**) Coomassie-stained 4–12% SDS-PAGE of the HMTase reactions shown in *Figure 3C*. *Drosophila*

*Figure 3—figure supplement 1 continued on next page*

*melanogaster* (*D.m.*) nucleosomes were used for these experiments. The short 5 kDa PHF$_C$ fragment is not visible on this gel. (**B**) Full ESI MS spectra (upper part) and full deconvoluted MS spectra (lower part) shown for input peptides without PRC2 as a control (left) and with PRC2 (right) to ensure no overlapping between possible adduct peaks and monomethylation peaks. (**C**) Western blot (WB) analysis of HMTase reactions with full-length PHF1-PRC2 on unmodified (lanes 1–4) or H3Kc36me3 (lanes 5–7) mononucleosomes (446 nM).
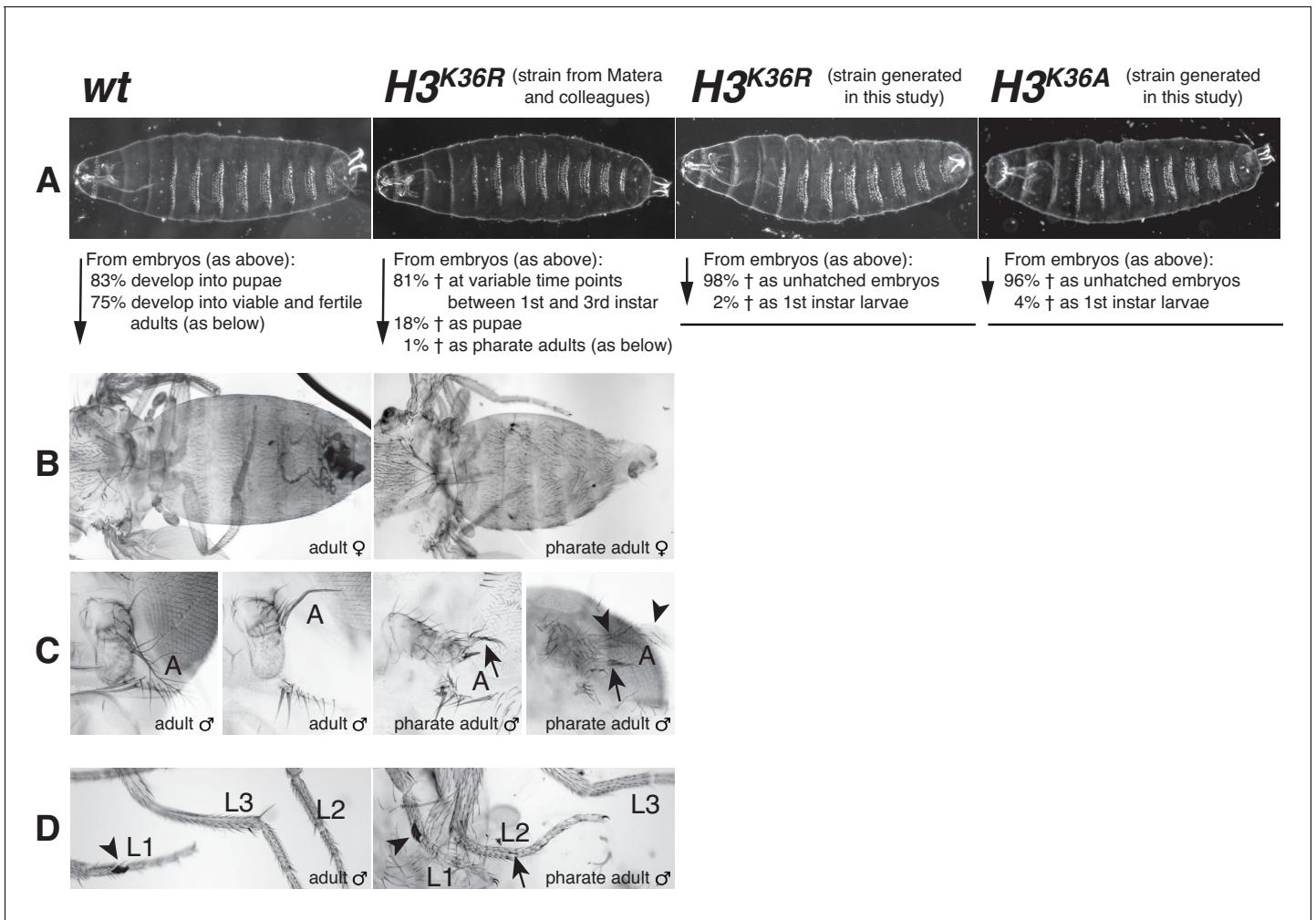
**Figure 4.** *Drosophila* with H3^K36R or H3^K36A mutant chromatin arrest development after completion of embryogenesis. (**A**) Ventral views of cuticles from *wildtype* (*wt*), *H3^K36R*, or *H3^K36A* mutant embryos. Note that the cuticle pattern of the mutant animals is indistinguishable from that of the *wt* embryo. Below: for each genotype, the fraction of embryos that developed into larvae, pupae, pharate adults or viable adults is listed. The fraction was determined by monitoring the development of collected hatched 1$^{st}$ instar larvae (*wt*: $n = 300$, *H3^K36R* (Matera strain): $n = 2000$) or unhatched embryos (*H3^K36R* (strain generated in this study): $n = 200$; *H3^K36A*: $n = 200$). The GFP marker on the Balancer chromosomes was used for identifying *H3^K36R* and *H3^K36A* mutants. See Materials and methods for further information and discussion. (**B**) Dorsal views of the posterior portion of the thorax and of the abdomen. From 2000 hatched *H3^K36R* mutant 1$^{st}$ instar larvae, a total of 18 pharate adults was recovered. Most *H3^K36R* mutant pharate adults showed a relatively normal overall body patterning apart from the homeotic transformations illustrated below. (**C**) Frontal view of adult heads illustrating the antenna-to-leg transformation in *H3^K36R* mutant pharate adults. The antenna-to-leg transformation in *H3^K36R* mutant animals ranged from mild (arrows) to more extensive transformations with formation of leg-like structures such as in this extreme case (arrowheads). (**D**) The sex comb in males is normally only present on the protoracic (**L1**) legs (arrowheads). Among the *H3^K36R* mutant pharate adult males recovered ($n = 13$), five showed one or several extra sex comb teeth (arrow) on the meso- (**L2**) or meta-thoracic (**L3**) legs. Extra sex comb teeth in adults are a hallmark phenotype of polycomb mutants.
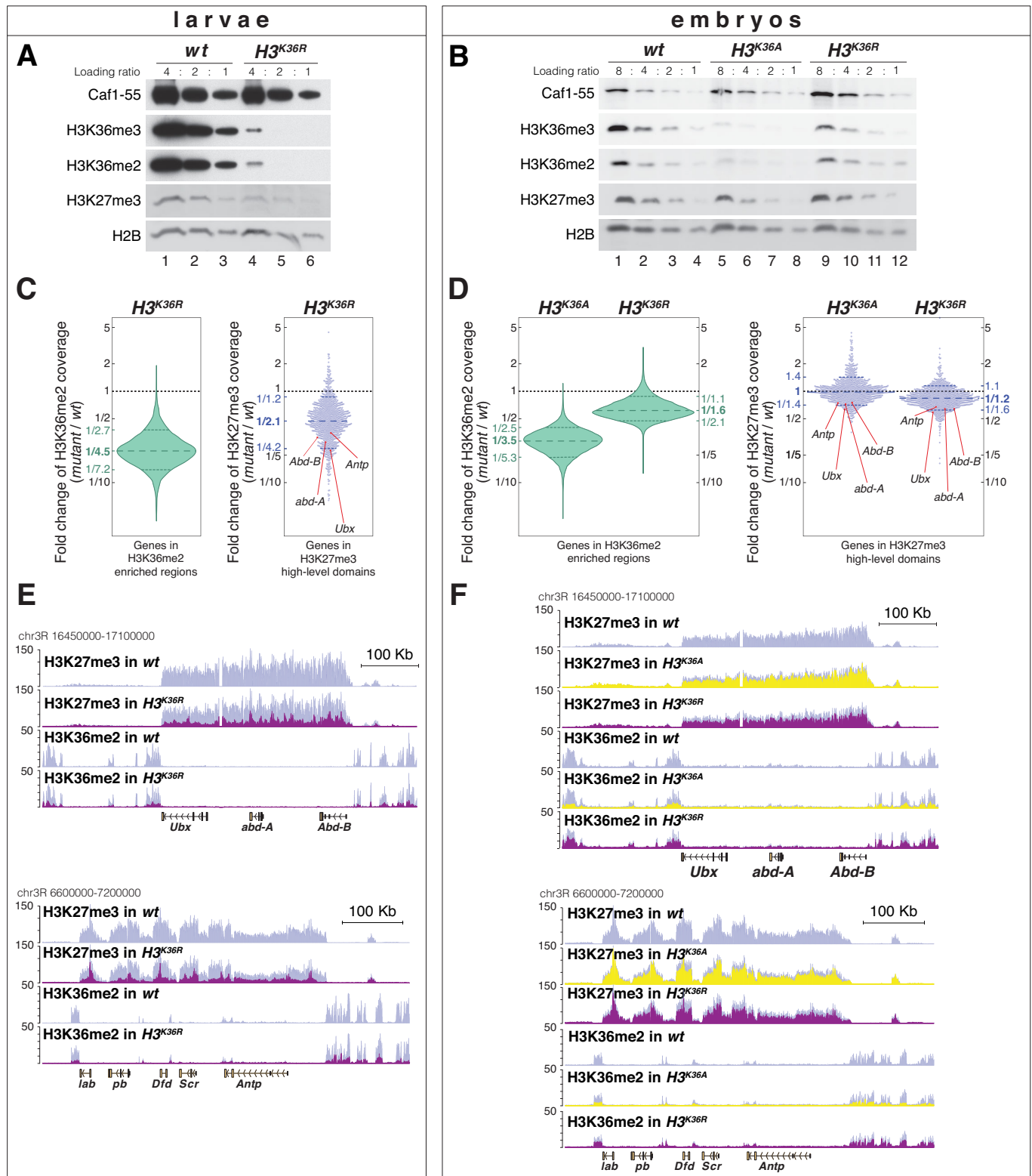
**Figure 5.** $H3^{K36A}$ and $H3^{K36R}$ mutants show reduced levels of H3K27me3. (**A**) Western blot analysis on serial dilutions (4:2:1) of total cell extracts from wing, haltere and 3rd leg imaginal disc tissues dissected from *wildtype* (*wt*, lanes 1–3) and $H3^{K36R}$ mutant (lanes 4–6) third instar larvae. Blots were

*Figure 5 continued on next page*

*Figure 5 continued*

probed with antibodies against H3K36me3, H3K36me2, or H3K27me3; in each case, probing of the same membranes with antibodies against Caf1-55 and H2B served as controls for loading and western blot processing. Note the reduced levels of H3K36me3 and H3K36me2 but also of H3K27me3 in $H3^{K36R}$ mutants compared to *wildtype* (*wt*) (see text). See Materials and Methods for details of all genotypes. (**B**) Western blot analysis on serial dilutions (8:4:2:1) of total nuclear extracts from 21 to 24 hr old *wt* (lanes 1–4), $H3^{K36A}$ mutant (lanes 5–8) and $H3^{K36R}$ mutant (lanes 9–12) embryos, probed with antibodies against H3K36me3, H3K36me2 or H3K27me3; and with antibodies against Caf1-55 and H2B as controls. Note that H3K36me3 and H3K36me2 levels are reduced in $H3^{K36A}$ mutants but not in $H3^{K36R}$ mutants where they are comparable to *wt*. Also note that H3K27me3 levels appear undiminished in either mutant (see text). (**C**) Left, violin plot showing the fold-change of H3K36me2 coverage in $H3^{K36R}$ mutant larvae relative to *wt* at genes that in *wildtype* larval CNS and imaginal disc tissues are decorated with H3K36me2 (see Materials and Methods). The dashed line marks the median reduction (4.5-fold), the dotted lines indicate the interval comprising 80% of regions. Right, Bee plot showing the fold-change of H3K27me3 coverage in $H3^{K36R}$ mutant larvae relative to *wt* at genes that in *wildtype* larval CNS and imaginal disc tissues are associated with high-level H3K27me3 regions (see Materials and Methods). The dashed line marks the median reduction (2.1-fold), the dotted lines indicate the interval comprising 80% of regions. Note that H3K27me3 coverage at the HOX genes *abd-A*, *Abd-B*, *Ubx* and *Antp* is between 3- and 4-fold reduced. (**D**) Analysis and representation as in (**C**) but showing fold-changes in H3K36me2 and H3K27me3 coverage in $H3^{K36A}$ and $H3^{K36R}$ mutant late-stage embryos relative to *wt* at genes that in *wildtype* embryos are decorated with H3K36me2 and H3K27me3, respectively. Note that H3K27me3 coverage at the HOX genes *abd-A*, *Abd-B*, *Ubx* and *Antp* is about 1.5-fold reduced. See also ***Figure 5—figure supplement 1***. (**E**) H3K27me3 and H3K36me2 ChIP-seq profiles in larval CNS and imaginal disc tissues from *wt* (blue) and $H3^{K36R}$ mutant (purple) third instar larvae; in the tracks showing the profiles in the $H3^{K36R}$ mutant, the *wt* profile is superimposed as reference (see ***Supplementary file 2*** and Materials and Methods for information about normalization). Top: genomic interval containing the *Bithorax-Complex* harboring the HOX genes *Ubx*, *abd-A* and *Abd-B*; bottom: genomic interval containing the *Antennapedia-Complex* with the HOX genes *lab*, *pb*, *Dfd*, *Scr*, and *Antp*. Note the 3- to 4-fold reduction of H3K27me3 levels across the *Bithorax* and *Antennapedia* loci in $H3^{K36R}$ mutants. Also note that for every HOX gene, the analyzed tissues (CNS, thoracic imaginal discs and eye-antenna discs) represent a mixed population of cells with a fraction of cells in which the gene is inactive, decorated with H3K27me3 and repressed by PcG and fraction of cells in which the gene is transcriptionally active and carrying the H3K36me2 modification. (**F**) H3K27me3 and H3K36me2 ChIP-seq profiles at the Bithorax and Antennapedia loci as in (**E**) but from *wt* (blue), $H3^{K36A}$ mutant (yellow) and $H3^{K36R}$ mutant (purple) late-stage embryos with the *wt* profile superimposed in the tracks showing the profiles in the $H3^{K36A}$ and $H3^{K36R}$ mutants. H3K27me3 levels across the Bithorax and Antennapedia loci in $H3^{K36A}$ and $H3^{K36R}$ mutants are only about 1.5-fold reduced compared to *wt*.
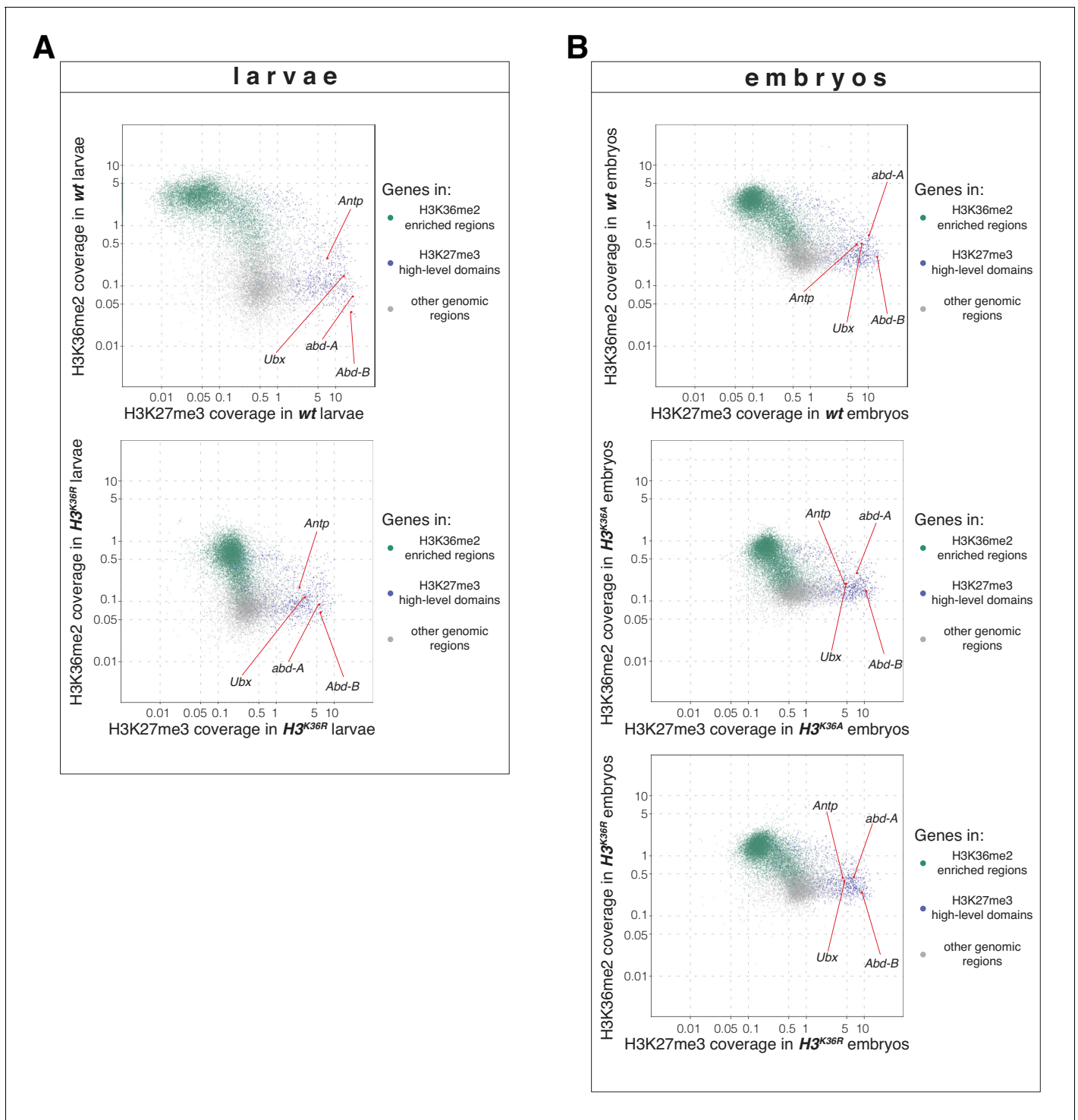
**Figure 5—figure supplement 1.** *H3*$^{K36R}$ and *H3*$^{K36A}$ mutants show altered H3K36me2 and H3K27me3 profiles (related to *Figure 5*). (**A**) Top, scatter plots showing H3K36me2 coverage in relation to H3K27me3 coverage in *wt* larvae. Green dots represent 9200 gene bodies overlapping with genomic intervals showing H3K36me2 enrichment, blue dots represent 1030 gene bodies overlapping with genomic intervals defined as high-level H3K27me3 domains (*Bonnet et al., 2019*), and gray dots represent 6300 gene bodies showing no enrichment for either methylation mark in larvae (see Materials and Methods). Bottom, scatter plot showing the H3K36me2 read coverage in relation to H3K27me3 read coverage in *H3*$^{K36R}$ mutant larvae. (**B**) As in (**A**) but showing H3K36me2 coverage in relation to H3K27me3 coverage in *wt* embryos (top), in *H3*$^{K36A}$ mutant embryos (middle) and in *H3*$^{K36R}$ mutant embryos (bottom). Green dots represent 10800 gene bodies overlapping with genomic intervals showing H3K36me2 enrichment, blue dots represent 1030 gene bodies overlapping with genomic intervals defined as high-level H3K27me3 domains (*Bonnet et al., 2019*), and gray dots represent 5400 gene bodies showing no enrichment for either methylation mark in embryos (see Materials and methods).
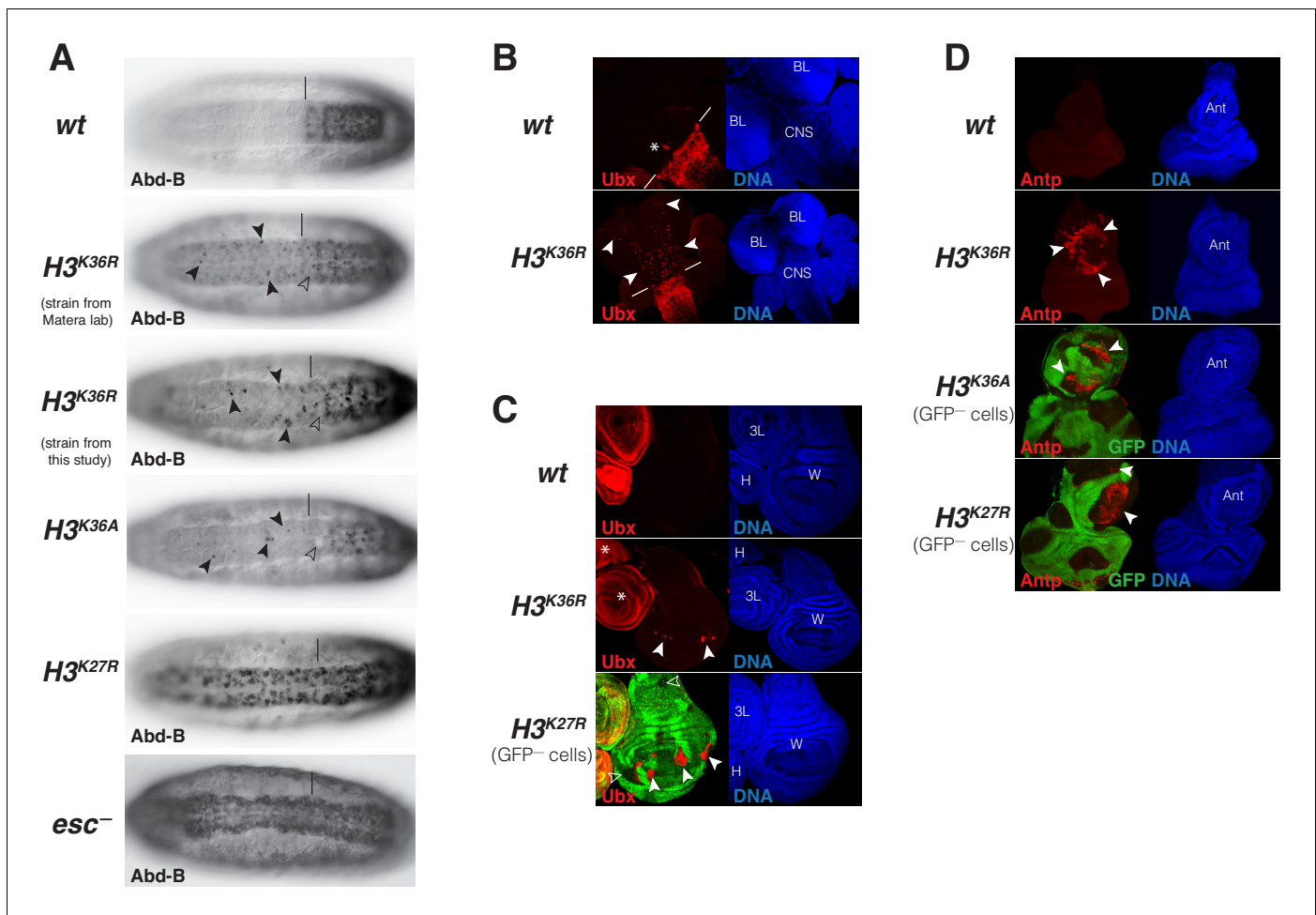
**Figure 6.** *Drosophila* with H3K36R or H3K36A chromatin show defective Polycomb repression at HOX genes. (**A**) Ventral views of stage 16 *wildtype* (*wt*), H3K36A, H3K36R, H3K27R, or *esc* (*esc⁻*) mutant embryos, stained with antibody against Abd-B protein; the *esc* mutant embryo lacked both maternal and zygotic expression of *esc* (see Materials and Methods for details of all genotypes). The vertical bar marks the anterior boundary of *Abd-B* expression in parasegment (ps) 10 in *wt* embryos. Note the stochastic misexpression of Abd-B protein in single cells or pairs of cells anterior to ps10 in H3K36R and H3K36A mutant embryos (arrowheads). H3K27R and *esc* mutant embryos show widespread misexpression of Abd-B protein in the head-to-tail pattern characteristic of PcG mutants. For reasons that are not well understood, H3K36A and H3K36R mutants also show partial loss of Abd-B expression in cells in ps10 (empty arrowheads). (**B**) Larval CNS and brain lobe tissues from *wildtype* (*wt*) or H3K36R mutant third instar larvae, stained with antibody against Ubx protein (red) and Hoechst (DNA) to label all nuclei; location of CNS and brain lobes (BL) are indicated in the right panel. The white bars mark the anterior boundary of *Ubx* expression in ps5 in *wt* embryos, the asterisk marks the Ubx-expressing cells in the central midline of ps4 that are part of the wild-type Ubx pattern. Note the stochastic misexpression of Ubx protein in many single cells anterior to ps5 in the CNS and in the brain lobes (arrowheads). (**C**) Imaginal wing (**W**), haltere (**H**) and 3rd leg (3L) discs from *wildtype* (*wt*) or H3K36R mutant third instar larvae and, as reference, discs from a larvae with clones of H3K27R mutant cells that are marked by the absence of GFP. In all cases, discs were stained with antibody against Ubx protein (red) and Hoechst (DNA) to label all nuclei. In *wt* animals, Ubx is expressed in the haltere and 3rd leg disc but not in the wing disc where it is repressed by the PcG machinery. Note that in H3K36R mutants, Ubx is misexpressed in small clusters of cells in the wing blade primordium of the wing disc (arrowheads) but remains repressed in the rest of the wing disc. Such misexpression was detected in 50% of wing discs (n = 28). As reference, a wing discs with H3K27R mutant clones is shown, where all cells in the clones in the wing blade primordium (arrowheads) show misexpression of Ubx whereas cells in the notum and hinge primordium show no misexpression (empty arrowheads) (cf. *Pengelly et al., 2013*). Also note that in H3K36R mutants (n > 30 mutant animals analyzed), Ubx expression in haltere and leg discs appears unperturbed (asterisks). (**D**) Eye-antennal imaginal discs from *wildtype* (*wt*) or H3K36R mutant larvae and below discs from larvae with clones of H3K36A or H3K27R mutant cells that are marked by the absence of GFP. All animals were stained with antibody against Antp protein (red) and Hoechst (DNA) to label all nuclei. Antp is not expressed in the eye-antennal disc of *wt* animals. Note that in H3K36R mutant discs, Antp is misexpressed in large clusters of cells (arrowheads) in the antenna primordium (Ant). Note that Antp is also misexpressed in H3K36A or H3K27R mutant cell clones in the antenna primordium (arrowheads) and that in these cases misexpression also only occurs in a subset of the mutant cells and not in all clones.
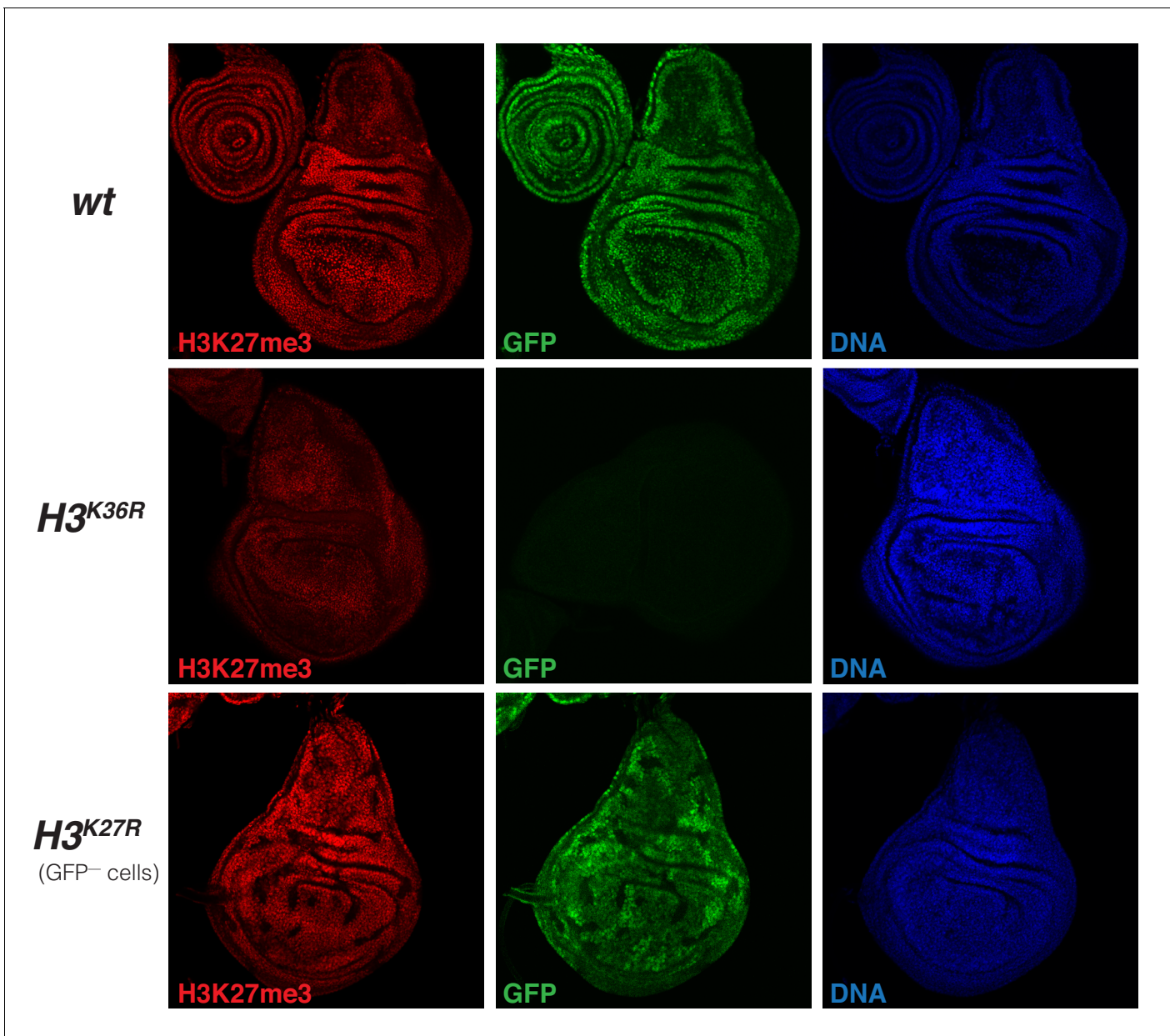
**Figure 6—figure supplement 1.** H3K27me3 levels are uniformly reduced in imaginal disc tissues from $H3^{K36R}$ mutant larvae (related to *Figure 6*). Imaginal wing discs from *wildtype* (*wt*) or $H3^{K36R}$ mutant third instar larvae and, as reference, from a larva with clones of $H3^{K27R}$ mutant cells that are marked by the absence of GFP. In all cases discs were stained with antibody against H3K27me3 (red), and with Hoechst (DNA) to label all nuclei. The discs from *wt* larvae, marked by GFP in all nuclei, and $H3^{K36R}$ mutant larvae, marked by the absence of GFP signal, come from preparations where larvae of the two genotypes were formaldehyde-fixed and antibody-labeled in the same vial, mounted on the same slide and photographed by confocal microscopy with identical exposure settings. Note that the H3K27me3 immunofluorescence signal appears uniformly reduced across the tissue. These are a single confocal section across a disc and not all nuclei are in exactly the same focal plane, accounting for some differences in signal intensity across the images. The wing disc with clones of $H3^{K27R}$ mutant cells, marked by the absence of GFP, is shown as reference for the specificity of the H3K27me3 antibody signal.